Natural Resources for Human Health

visagaa publishing house

Original Research

View Article online

Check for updates

Received 24 November 2025
Revised 16 January 2025
Accepted 16 June 2026
Available Online 11 August 2026

Edited by Kannan RR Rengasamy

KEYWORDS:
Molecular docking
Cytochrome P450 2E1
Free energy calculation
Satureja hortensis
Urethane-induced mutagenesis

Natr Resour Human Health 2026; 6 (4): 243–263
https://doi.org/10.53365/nrfhh/224628
eISSN: 2583-1194

In-silico discovery of CYP2E1 inhibitors from Satureja hortensis L. for urethane-induced mutagenesis: Molecular docking to MD simulation and MM/GBSA energy calculation

Vindya NS[1,2], Syed Sagheer Ahmed[2*], Bharathi DR[2]

[1]Department of Pharmacology, Al-Ameen College of Pharmacy, Bengaluru – 560027, India
[2]Department of Pharmacology, Faculty of Pharmacy, Sri Adichunchanagiri College of Pharmacy, Adichunchanagiri University, B.G. Nagara – 571448, India

ABSTRACT: *Backgrounds*: Urethane is a potent environmental mutagen whose bioactivation is primarily mediated by cytochrome P450 2E1 (CYP2E1). The phytoconstituents of Satureja hortensis L. have been traditionally recognized for their medicinal value, but their molecular interactions with CYP2E1 remain underexplored. *Methods*: Approximately 360 phytochemicals were retrieved from the IMPPAT database, duplicates and non-drug-like molecules were filtered, and drug-likeness properties were evaluated using ADMETLab 3.0. Molecular docking, molecular dynamics (MD) simulation (100 ns), free energy landscape (FEL) mapping, and binding free energy calculations were performed to characterize CYP2E1–ligand interactions. *Results*: Drug-likeness profiling screened the phytoconstituents for molecular docking study. Docking predicted stable binding affinity (–8.6 kcal/mol) of alpha-curcumene in the CYP2E1 active pocket through hydrophobic and π–π interactions with PHE46, TRP214, LEU217, and LEU228. MD simulations confirmed the dynamic stability of the complex with minimal deviations and stable solvent-accessible properties. FEL and principal component analysis (PCA) revealed confinement of the complex to low-energy conformational states. The binding free energy (ΔG_bind = –75.31 ± 3.1 kcal/mol) was dominated by van der Waals and lipophilic interactions, corroborating its strong binding affinity. Comparative analysis showed alpha-curcumene to be more stable and energetically favorable than other S. hortensis phytoconstituents. *Conclusion*: Integrated computational analysis demonstrates that alpha-curcumene from S. hortensis L. exhibits strong and stable interaction with CYP2E1, suggesting a mechanistic basis for its potential protective role against urethane-induced mutagenesis. These findings position alpha-curcumene as a promising bioactive candidate, warranting further in vitro and in vivo validation.

* Corresponding author.
E-mail address: sagheer@accp.co.in (Syed Sagheer Ahmed)

GRAPHICAL ABSTRACT

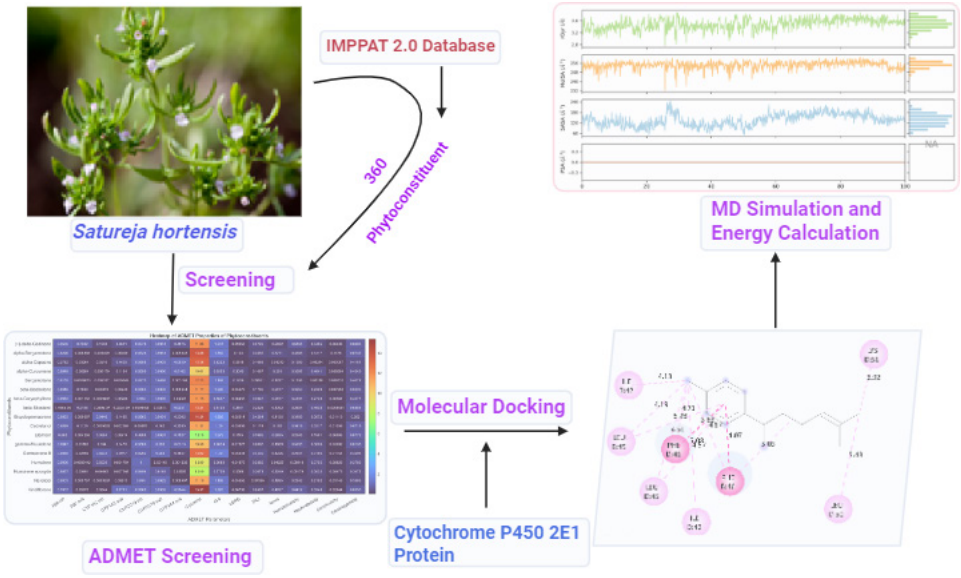

1. INTRODUCTION

Urethane (ethyl carbamate) is a naturally occurring and industrially produced compound that has been classified as a Group 2A carcinogen by the International Agency for Research on Cancer (IARC), indicating probable carcinogenicity in humans (Zuckerman, 1995). Its carcinogenic potential is well-documented, with studies demonstrating its ability to induce tumors in various organs across multiple animal species (Park et al., 2009). The primary mechanism underlying urethane's carcinogenicity involves its metabolic activation into reactive intermediates that can covalently bind to cellular macromolecules, particularly DNA, leading to the formation of mutagenic adducts. This DNA damage, if not properly repaired, can result in mutations that initiate the process of carcinogenesis (Schlatter and Lutz, 1990; Sozio et al., 2021).

The metabolism of urethane and many other xenobiotics is largely orchestrated by the Cytochrome P450 (CYP) superfamily of enzymes (Figure 1), which are critical for the detoxification or, in some cases, the bioactivation of foreign compounds (Iacopetta et al., 2023). Among these, human Cytochrome P450 2E1 (CYP2E1) has been identified as a significant enzyme involved in the metabolic activation of urethane. CYP2E1 can catalyze the hydroxylation of urethane, leading to the formation of the highly reactive vinyl carbamate intermediate (Garciá-Suástegui et al., 2017). This intermediate readily decomposes to generate reactive species capable of causing DNA damage and promoting mutagenesis. Therefore, understanding and modulating the activity of CYP2E1 presents a promising strategy for mitigating urethane's mutagenic and carcinogenic effects (Oliveira et al., 2020).

In the pursuit of natural chemopreventive agents, medicinal plants have garnered significant attention due to their rich biodiversity of bioactive compounds with therapeutic potential. *Satureja Hortensis* L., commonly known as summer savory, is a medicinal herb traditionally used for its various pharmacological properties, including antioxidant, anti-inflammatory, and antimicrobial activities (Chambre et al., 2020; Kumburovic et al., 2020). The therapeutic benefits of *S. Hortensis* L. are attributed to its phytochemicals, which include flavonoids, phenolic acids, and terpenoids (Fierascu et al., 2018). The study also revealed that *S. Hortensis* extract inhibits cancer cell proliferation (Vladić et al., 2020). Given the known role of CYP2E1 in urethane mutagenesis and the ethnobotanical evidence for the protective effects of various plant extracts, it is plausible that the phytoconstituents of *S. Hortensis* L. may possess inhibitory activity against CYP2E1, thereby offering a protective mechanism against urethane-induced mutagenesis.

This study aims to investigate the potential of selected phytoconstituents from *S. Hortensis* L. to counteract urethane-induced mutagenesis by targeting human CYP2E1. Utilizing a multifaceted computational approach, we first employed molecular docking to predict the binding affinities and interaction modes of these phytoconstituents with the CYP2E1 active site. That was followed by extensive molecular dynamics (MD) simulations to assess the stability and

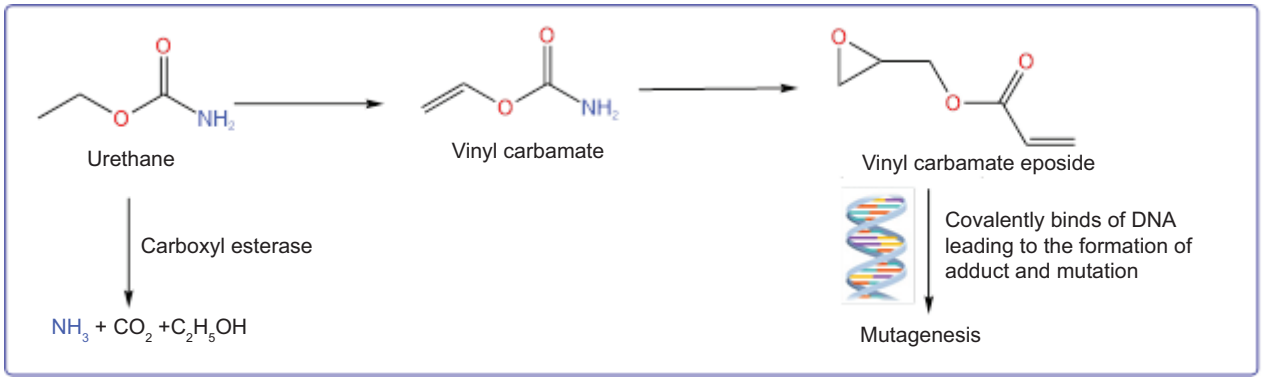

Figure 1. Urethane metabolism and carcinogenic action (Sozio et al., 2021).

dynamic behavior of these ligand–protein complexes over 100 ns. Finally, molecular mechanics/generalized born surface area (MM/GBSA) energy calculations were performed to provide a more accurate estimation of the binding free energies. By integrating these computational techniques, this research seeks to identify promising phytoconstituents from *S. Hortensis* L. that can inhibit CYP2E1, offering a molecular basis for its potential role in preventing urethane-induced mutagenesis and contributing to the development of novel, naturally derived chemopreventive strategies.

2. MATERIALS AND METHODS

2.1. Phytoconstituents retrieval

A total of 360 phytoconstituents of *S. hortensis* L. were retrieved from the IMPPAT 2.0 (Indian Medicinal Plants, Phytochemistry and Therapeutics) database (Vivek-Ananth et al., 2023). Duplicate entries were removed, yielding 170 unique phytoconstituents. Nonrelevant classes such as amino acids, aliphatic hydrocarbons, and fatty acids were excluded, as these do not generally qualify as drug-like scaffolds. The remaining phytoconstituents were subjected to in silico screening to assess their drug-likeness and pharmacokinetic potential.

2.2. Selection criteria

Selection criteria for drug-likeness were based on compliance with Lipinski's Rule of Five (Ivanović et al., 2020), absence of pan-assay interference compounds (PAINS) alerts, and a toxicity score below 0.7 (Baell and Nissink, 2018). Physicochemical parameters, including molecular weight (MW), LogP, topological polar surface area (TPSA), hydrogen bond donors and acceptors, and CaCO-2 permeability, were calculated (Saritha, et al., 2024)

2.3. Pharmacokinetic and toxicity prediction

The pharmacokinetic and toxicity properties (ADMET) of the shortlisted compounds were predicted using ADMETLab 3.0 (https://admetmesh.scbdd.com/) (Xiong et al., 2021). Parameters analyzed included absorption (CaCO-2 permeability, human intestinal absorption (HIA), P-glycoprotein (P-gp) substrate/inhibition, blood–brain barrier penetration), distribution (plasma protein binding (PPB), volume of distribution), metabolism (CYP450 isoform inhibition and substrate prediction), excretion (total clearance, half-life), and toxicity endpoints (hERG cardiotoxicity, Ames mutagenicity, hepatotoxicity, nephrotoxicity, genotoxicity, and carcinogenicity) (Kamaria et al., 2025).

2.4. Heatmap visualization

The predicted data for 17 phytoconstituents were visualized using MATLAB R2024b in the form of heatmaps to compare drug-likeness and ADMET properties across phytoconstituents, enabling the systematic identification of promising candidates for molecular docking and MD simulations.

2.5. Molecular docking procedure

2.5.1. Selection of phytoconstituents

A critical step involved the selection of phytoconstituents. Seventeen phytoconstituents were chosen from the IMPPAT database 2.0, specifically from the plant *S. Hortensis* L., based on a preliminary screening that evaluated their absorption,

distribution, metabolism, excretion, and toxicity (ADMET) properties, alongside their adherence to Lipinski's Rule of Five to ensure potential drug-likeness. Three-dimensional structures for these selected phytoconstituents were retrieved from PubChem in SDF format (Pant et al., 2024). Each of these ligands, as well as the co-crystal ligand pilocarpine and the reference drug 4-methylpyrazole, underwent a preparation process that included energy minimization (MMFF94 force field), assigning Gasteiger partial charges, defining their atom types, and converting into PDBQT using OpenBabel v3.1.1 software (Thapa et al., 2023).

2.5.2. Protein preparation

The three-dimensional structure of human Cytochrome P450 2E1 (3T3Z) was retrieved from the Protein Data Bank (PDB) (DeVore et al., 2012). CYP2E1 is a key enzyme in the cytochrome P450 superfamily, primarily responsible for the oxidative metabolism of a wide range of endogenous and exogenous substances (Reed et al., 2018). Notably, it plays a significant role in the metabolic activation of several known mutagens and carcinogens, transforming them into reactive intermediates that can damage DNA and initiate the process of mutagenesis (Guengerich, 2020). Subsequent preparation involved using AutoDock MGL Tool v1.5.7 software to remove water molecules and nonessential heteroatoms, thereby streamlining the structure for docking. Polar hydrogen and Kollmann charges were assigned to the protein, and AD4 atom types were defined to facilitate accurate energetic calculations (Thapa, Nargund, and Biradar, 2023). To ensure the stereochemical integrity of the protein model, its quality was rigorously assessed using a Ramachandran plot, confirming the correct conformation of amino acid residues (Gote et al., 2025).

2.5.3. Binding site identification and grid generation

The active site of the 3T3Z enzyme was identified by examining the location of the co-crystal ligand, pilocarpine, within the protein structure. Based on this identification, a grid box was generated to precisely encompass this active site. The coordinates for the center of this grid box were determined to be x = 58.59, y = −22.92, and z = 31.75. The dimensions and central coordinates of this grid box were carefully set to ensure thorough exploration of all possible ligand binding poses within the defined region, facilitating an exhaustive docking search.

2.5.4. Molecular docking

Molecular docking simulations were carried out using the AutoDock Vina v1.2.0 software (Trott and Olson, 2009). The prepared protein structure, serving as the receptor, and the PDBQT-formatted structures of the phytoconstituents, pilocarpine, and 4-methylpyrazole, acting as ligands, were used as input. The software was configured to perform an exhaustive search for the most energetically favorable binding poses of each ligand within the predefined grid box (Joshi et al., 2025). For each successful ligand–protein complex, docking scores, which represent the predicted binding affinity in kcal/mol, were recorded; lower (more negative) scores indicate stronger binding.

2.5.5. Analysis of docking results

The outcomes of the molecular docking were subjected to comprehensive analysis using BIOVIA Discovery Studio Visualizer 2021 software. The docking scores were used to rank the phytoconstituents based on their predicted binding affinities to 3T3Z, with compounds exhibiting more favorable (lower) scores being prioritized for further investigation. For selected top-scoring phytoconstituents, the 2D molecular interactions within the 3T3Z active site were visualized and analyzed. This detailed analysis involved identifying the specific amino acid residues that interacted with the ligands, characterizing the types of interactions (e.g., hydrogen bonds, hydrophobic interactions, pi-pi stacking, and pi-alkyl interactions), and measuring the distances at which these interactions occurred. Comparing these interaction patterns provided valuable insights into the potential mechanisms by which the phytoconstituents might modulate the activity of 3T3Z (Kumar et al., 2025).

2.5.6. Docking protocol validation through redocking

To ascertain the reliability of the docking protocol, a redocking experiment was performed in PyMol v3.1 (Pandey et al., 2024). A grid box was specifically generated around the binding site occupied by the co-crystal ligand, pilocarpine. Pilocarpine was then redocked into this defined pocket. The deviation between the original crystallographic pose of pilocarpine and the pose predicted by the docking software was quantified using the root-mean-square deviation (RMSD) (Prasad et al., 2025).

2.5.7. MD simulation

MD simulations were carried out using the Desmond module of Schrödinger release 2023–2024 to assess the stability and dynamic behavior of the protein–ligand complex (Thapa et al., 2024). "The protein–ligand complex obtained from docking studies was prepared using the Protein Preparation Wizard, where missing hydrogen atoms were added, bond orders were assigned, and hydrogen bonding networks were optimized. Energy minimization was performed with the OPLS4 force field to relieve steric clashes and optimize geometry. The system was solvated in an orthorhombic box using the TIP3P explicit water model, ensuring a buffer distance of at least 10 Å from the protein surface.

Counterions (Na^+ or Cl^-) were added to neutralize the system, followed by the addition of 0.15 M NaCl to mimic physiological ionic strength. The system was minimized using the steepest descent algorithm until a converged structure was obtained. Equilibration was performed in multiple steps under NPT ensemble conditions. The temperature of the system was gradually raised to 300 K using the Nose–Hoover thermostat, while pressure was maintained at 1.013 bar using the Martyna–Tobias–Klein barostat. The SHAKE algorithm was applied to constrain all bond lengths involving hydrogen atoms, allowing a 2 fs integration time step" (C et al., 2025).

2.5.8. Post-MD and MM/GBSA energy calculations

Production MD was carried out for 100 ns, with 1000 trajectory frames. Post-simulation analyses, including root mean square deviation (RMSD), root mean square fluctuation (RMSF), radius of gyration (rGyr), solvent-accessible surface area (SASA), hydrogen bonding, PCA, FEL, and MM/GBSA calculations, were performed using Desmond's simulation interaction diagram (SID) tool and the Prime MM/GBSA module of Schrödinger release 2023–2024 (Kiran et al., 2025).

3. RESULTS

3.1. Drug likeness and ADMET properties

The drug-likeness properties of phytoconstituents from *S. hortensis* L. are illustrated in Figure 2. Most compounds displayed MWs within the optimal drug-like range (200–225 Da), with beta-sitosterol (414.4 Da) as the only exception. Lipophilicity (logP) values were generally between 2.4 and 5.6, consistent with favorable passive permeability and oral absorption. Predicted HIA exceeded 90% for the majority of compounds, with alpha-curcumene and beta-bisabolene showing particularly high absorption potential. Predicted CaCO-2 permeability further supported good intestinal uptake. All compounds adhered to Lipinski's rule of five and were devoid of PAINS alerts, indicating a strong likelihood of drug-like behavior. PPB values were consistently high (>90%), suggesting extended systemic circulation, while distribution profiles indicated variable tissue penetration. Notably, alpha-bergamotene, elemicin, and bergamotene were predicted to cross the blood–brain barrier, suggesting possible neuromodulatory activity.

The ADMET evaluation (Figure 3) further strengthened the pharmacokinetic and safety profile of the compounds. P-gp interaction screening indicated that several constituents acted as nonsubstrates, reducing the likelihood of efflux-mediated drug resistance. In silico cytochrome P450 (CYP450) predictions revealed minimal inhibitory potential toward major isoforms (CYP1A2, CYP2C19, CYP2C9, and CYP3A4), indicating a low risk of metabolic interference. Compounds such as bicyclogermacrene and gamma-muurolene showed favorable metabolic stability with reduced clearance values. Toxicity endpoints, including Ames mutagenicity, hepatotoxicity, nephrotoxicity, and carcinogenicity, were largely negative, underscoring a broad safety margin.

Figure 2. Drug-likeness properties of phytoconstituents from *S. hortensis* L.

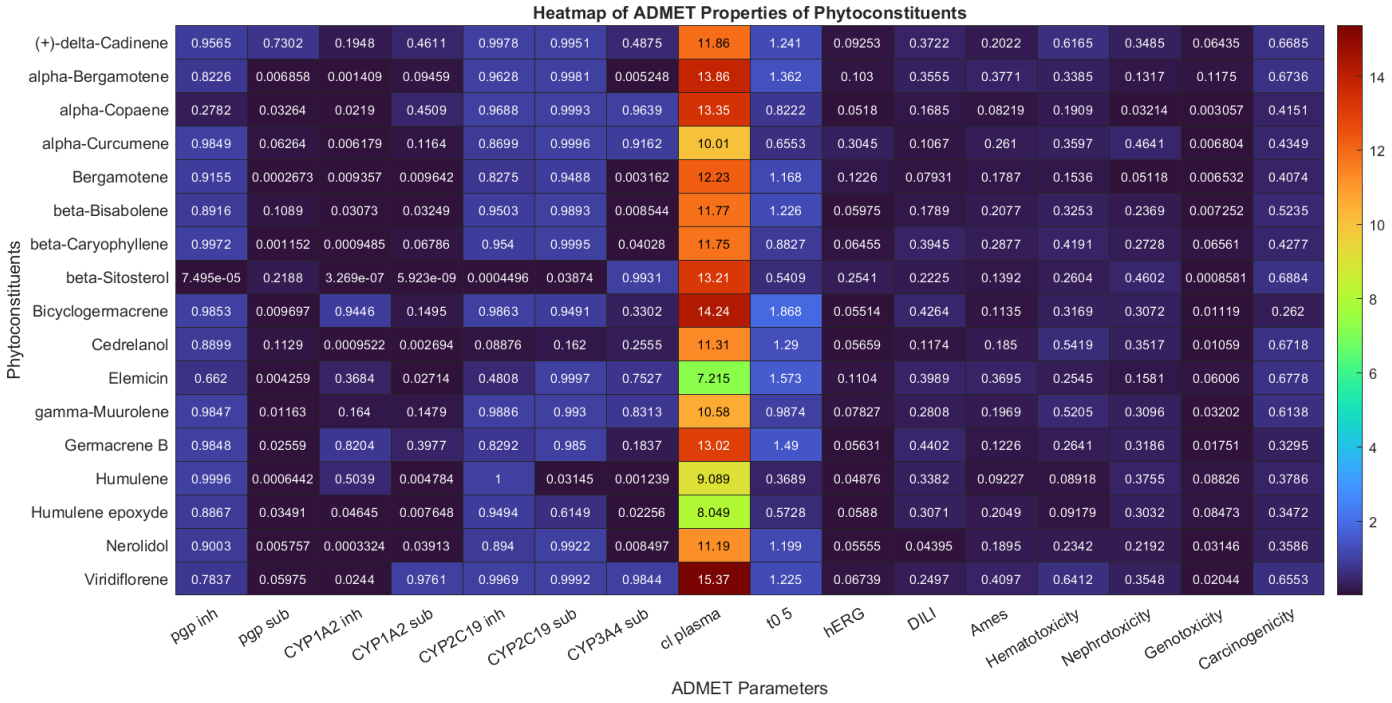

Figure 3. ADMET properties of phytoconstituents from *S. hortensis* L.

Elemicin and nerolidol demonstrated slightly elevated nephrotoxicity predictions, whereas viridiflorene exhibited higher predicted clearance, suggesting rapid systemic elimination. Importantly, no compound exhibited significant cardiotoxicity risk via hERG channel inhibition.

3.2. Molecular docking analysis

3.2.1. Validation of protein and docking protocol

The structural integrity of the human Cytochrome P450 2E1 (3T3Z) protein was confirmed through a Ramachandran plot (Figure 4A), where the majority of amino acid residues were found within the favored and allowed regions, indicating a high-quality protein model. Subsequently, the binding site of 3T3Z was successfully identified by focusing on the vicinity of the co-crystal ligand, pilocarpine, and a grid box was generated for docking (Figure 4B). The redocking of pilocarpine yielded a RMSD of 1.97Å when compared to its original pose (Figure 4C, green: co-crystal ligand, pink: redocked ligand), signifying the accuracy and reliability of the docking protocol employed.

3.2.2. Analysis of molecular docking results for phytoconstituents against 3T3Z

Molecular docking simulations were performed to assess the potential binding affinities of various phytoconstituents to the human Cytochrome P450 2E1 (3T3Z) enzyme, using pilocarpine as the co-crystal ligand and 4-methylpyrazole as a reference drug. The results, summarized in Table 1, reveal a range of binding affinities (−4.6 to −8.6 kcal/mol) among the tested compounds. Notably, alpha-curcumene exhibited the strongest binding affinity at −8.6 kcal/mol, followed closely by Germacrene B (−8.0 kcal/mol) and beta-Sitosterol (−7.7 kcal/mol). These values are significantly more favorable than those of the co-crystal ligand pilocarpine (−5.1 kcal/mol) and the reference drug 4-methylpyrazole (−4.5 kcal/mol), suggesting that these phytoconstituents may possess a higher potential for inhibiting CYP2E1 activity. Other compounds, including alpha-Bergamotene (−7.2 kcal/mol), Bergamotene (−7.3 kcal/mol), and beta-Bisabolene (−7.8 kcal/mol), also displayed considerable binding affinities, indicating their potential interaction with the enzyme's active site. Conversely, Elemicin (−5.7 kcal/mol), Humulene epoxyde (−6.1 kcal/mol), and gamma-Muurolene (−6.4 kcal/mol) showed weaker binding, suggesting a less pronounced interaction with 3T3Z. These findings highlight alpha-curcumene and Germacrene B as promising candidates for further investigation into their therapeutic potential related to CYP2E1 activity.

Further analysis of the molecular interactions revealed distinct binding modes for the top-scoring phytoconstituents. For alpha-curcumene (Figure 5A, B), the docking simulation indicated interactions with several amino acid residues, including PHE D:46, ILE B:42, LEU B:45, and LEU D:50,

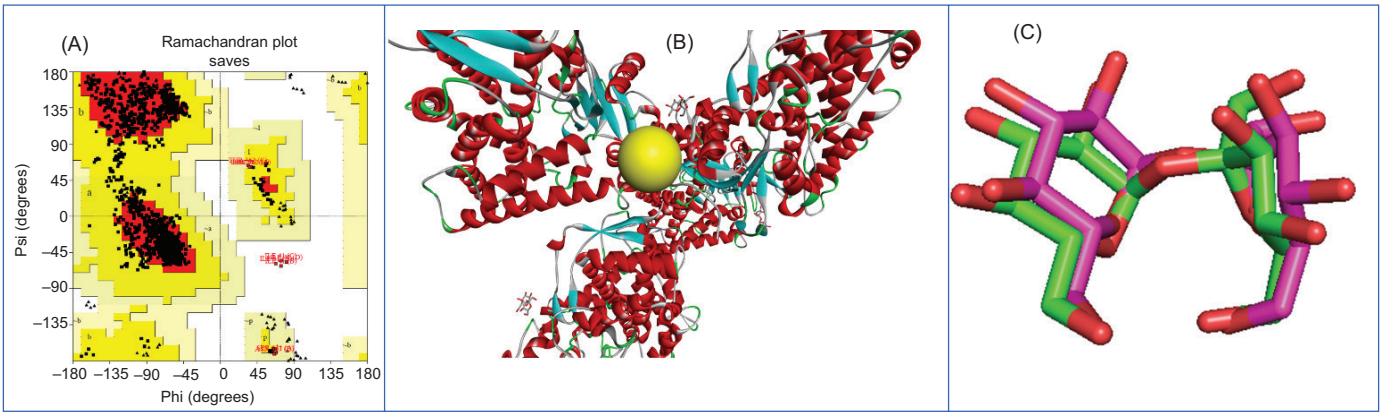

Figure 4. Validation of protein structure (A), binding site identification (B), and redocking accuracy (C).

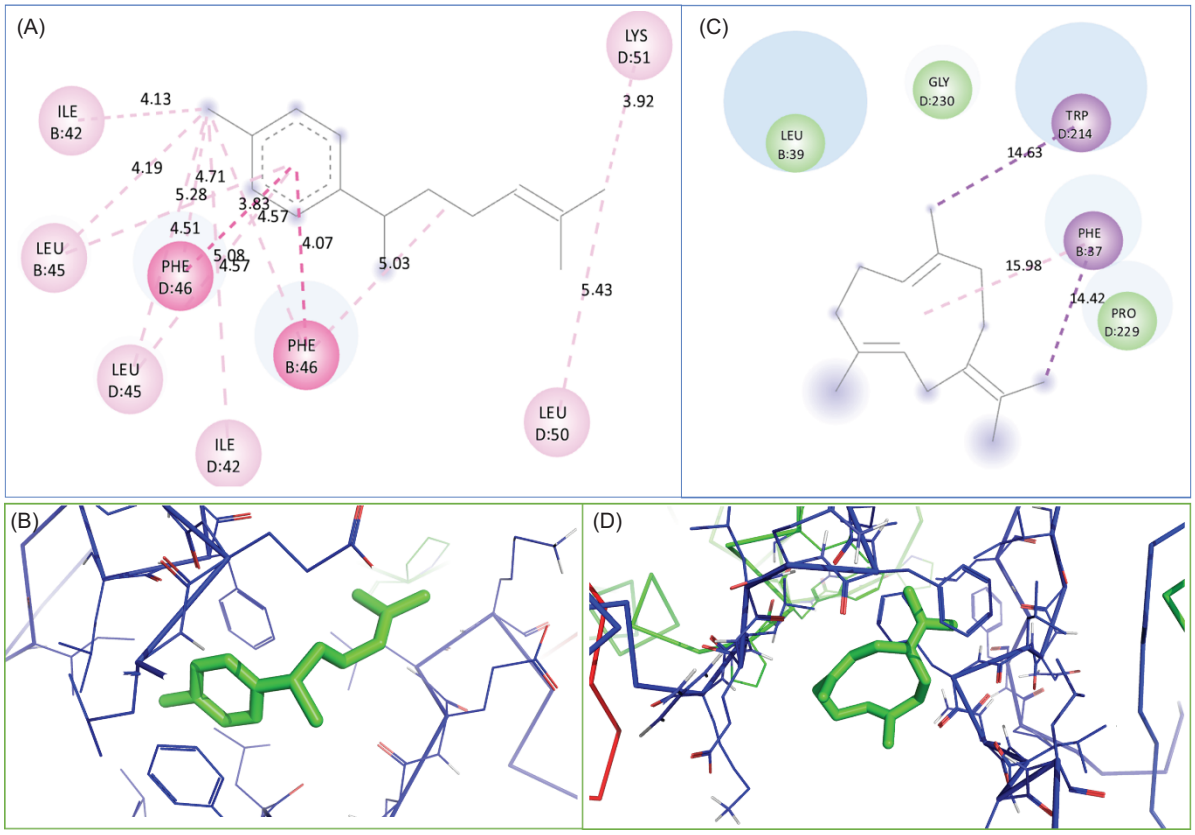

Figure 5. 2D and 3D molecular interaction of alpha-curcumene (A and B) and Germacrene B (C and D) against 3T3Z (Human Cytochrome P450 2E1). No hydrogen bond was observed in both the phytoconstituents.

with various interaction distances ranging from 4.07 to 5.28 Å, suggesting potential hydrophobic and van der Waals interactions. The aromatic ring of alpha-curcumene appears to engage in pi-pi stacking or hydrophobic interactions with PHE D:46, while its aliphatic chain likely interacts with leucine and isoleucine residues. In the case of Germacrene B (Figure 5C, D), the docking revealed a different set of interactions with 3T3Z. It appears to form interactions with residues such as TRP D:214, PHE B:37, PRO D:229, and LEU B:39. The interaction distances observed, such as 14.63 Å with TRP D:214 and 15.98 Å with PHE B:37, suggest potential involvement in larger binding pocket occupancy or different types of noncovalent interactions like pi-alkyl or hydrophobic contacts. The presence of interactions

Table 1
Molecular docking score, binding amino acid, and interaction of phytoconstituents against 3T3Z (Human Cytochrome P450 2E1 in complex with pilocarpine).

SN	Phytoconstituents	Binding affinity
1	(+)-Delta-Cadinene	−6.6
2	Allo-Aromadendrene	−6.7
3	Alpha-Bergamotene	−7.2
4	Alpha-Curcumene	−8.6
5	Bergamotene	−7.3
6	Beta-Bisabolene	−7.8
7	Beta-Caryophyllene	−6.6
8	Beta-Sitosterol	−7.7
9	Bicyclogermacrene	−6.6
10	Cedrelanol	−6.6
11	Elemicin	−5.7
12	Gamma-Muurolene	−6.4
13	Germacrene B	−8.0
14	Humulene	−6.5
15	Humulene Epoxyde	−6.1
16	Nerolidol	−6.7
17	Viridiflorene	−6.7
18	Co-Crystal Ligand (Pilocarpine)	−5.1
19	Reference Drug 4-Methylpyrazole	−4.5

with both aromatic (TRP D:214, PHE B:37) and aliphatic (LEU B:45, PRO D:229) residues highlights the adaptability of Germacrene B to the enzyme's active site.

Figure 6 illustrates the 2D molecular interactions of the co-crystal ligand pilocarpine and the reference drug 4-methylpyrazole with human Cytochrome P450 2E1 (3T3Z). Pilocarpine engages in multiple conventional hydrogen bonds with the enzyme. Specifically, it forms hydrogen bonds with GLN B:47 at distances of 2.05 Å and 3.04 Å, and with TRP D:214 at a distance of 2.47 Å (Figure 6A). These interactions, characterized by green dashed lines, suggest strong polar contacts that contribute significantly to pilocarpine's binding within the active site. In contrast, 4-methylpyrazole exhibits a different interaction profile. It primarily interacts with phenylalanine residues through pi-pi stacked and pi-alkyl interactions. The reference drug forms pi-pi stacked interactions with PHE B:46 (distance 4.12 Å) and PHE D:46 (distance 4.64 Å). In additionally, pi-alkyl interactions are observed with LEU D:45 (distance 4.50 Å) and PHE B:46 (distance 4.95 Å) (Figure 6B).

The two-dimensional interaction diagrams for the screened *Satureja hortensis* phytoconstituents consistently revealed a binding mode dominated by hydrophobic and aromatic contacts within the CYP2E1 active pocket (Supplementary Figures 1S–15S). Sesquiterpene and

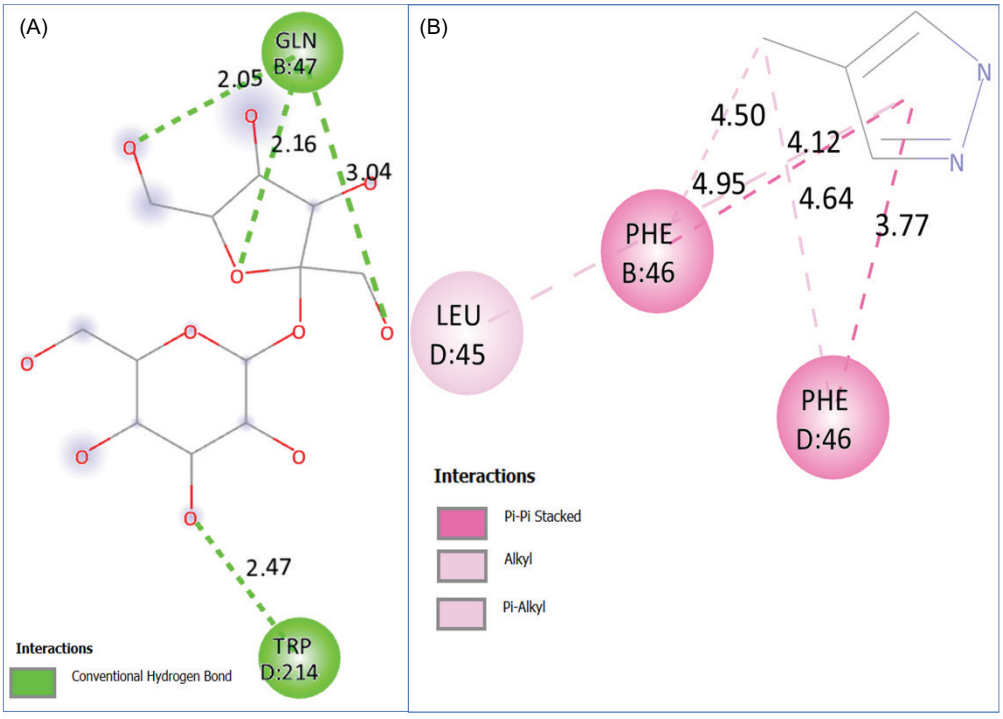

Figure 6. 2D molecular interactions of the co-crystal ligand pilocarpine (A) and the reference drug 4-methylpyrazole (B).

hydrocarbon scaffolds (e.g., α-curcumene, bicyclogermacrene, β-bisabolene, α-bergamotene, nerolidol) formed persistent van der Waals contacts and nonpolar packing with residues lining the hydrophobic cavity, while aromatic residues (notably TRP214 and PHE46 in multiple complexes) contributed recurrent π–π/ π/edge-to-face interactions that likely stabilize the ligand orientation.

3.2.3. MD simulation analysis

The MD simulation of the alpha-curcumene CYP2E1 complex (PDB ID: 3T3Z) was performed for 100 ns to assess the stability and conformational behavior of the ligand–protein interaction. The backbone RMSD profile (Figure 7A) demonstrated an initial equilibration phase followed by stabilization after ~20 ns, with fluctuations remaining within

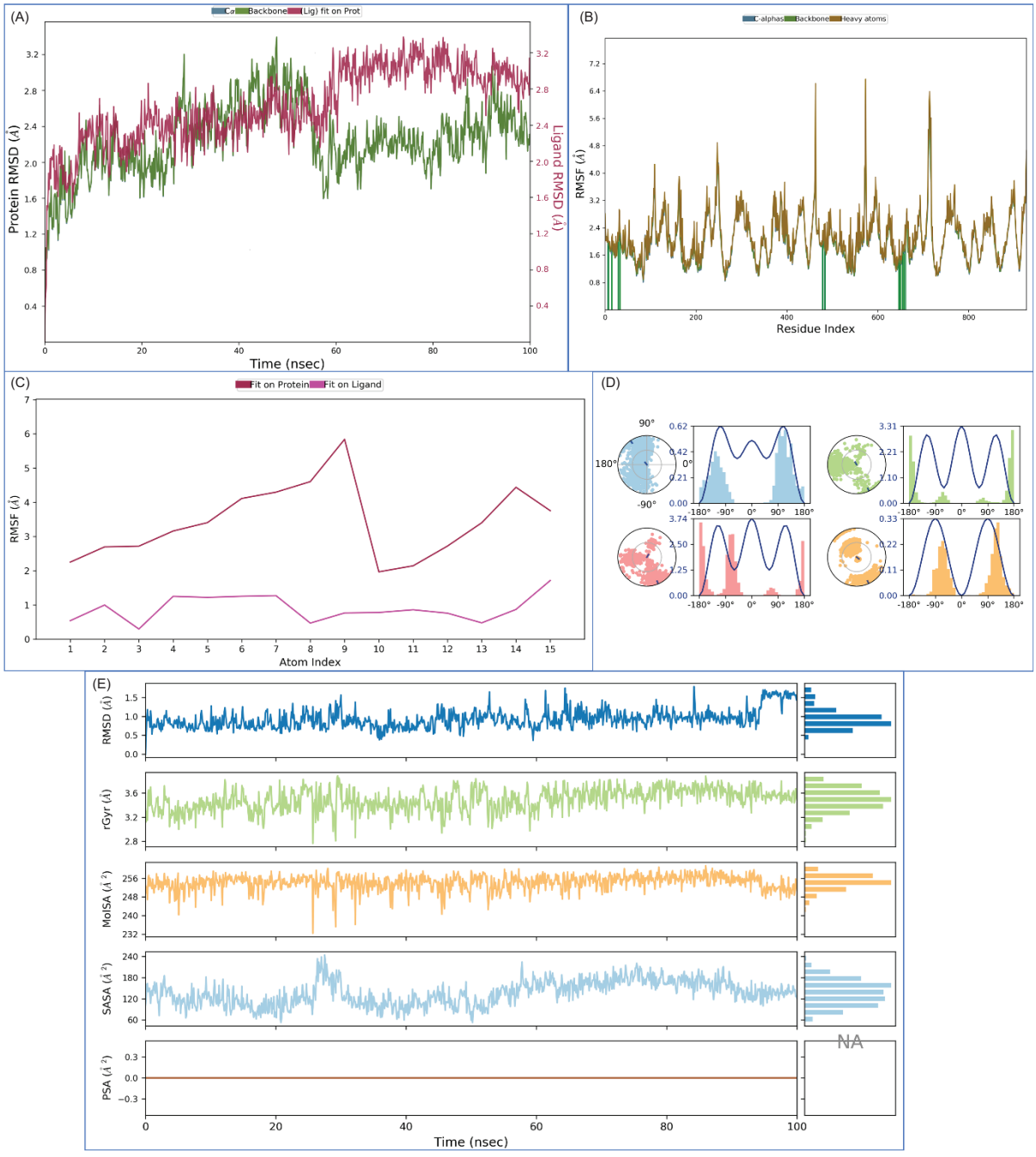

Figure 7. MD simulation of the 3T3Z-alpha-curcumene complex, showing protein–ligand RMSD (A), residue index and atomic fluctuation (RMSF) of the ligand and its interacting protein atoms (B & C), dihedral stability (D), and conformational and surface stability parameters of alpha-curcumene during simulation (E).

2.5–3.2 Å, suggesting a stable protein–ligand complex. The ligand RMSD, when fitted on the protein, exhibited minimal deviation, further confirming its consistent binding orientation within the active site.

The RMSF analysis of protein residues (Figure 7B) revealed localized flexibility at loop regions, while most catalytic residues remained relatively stable, indicating that ligand binding did not induce large-scale conformational instability. Secondary-structure element (SEE) profiling over the 100 ns trajectory showed that the global secondary structure of CYP2E1 remained largely conserved, with α-helices and β-sheets retaining their occupancy for the majority of the simulation; SEE histogram and timeline analyses indicate only short, localized transitions predominantly in loop regions flanking the active site (Supplementary Figures 16S & 17S). These transient local rearrangements coincide temporally with increased ligand contact in the same regions but do not translate into global unfolding or loss of structural integrity. Similarly, the ligand RMSF (Figure 7C) showed minor atomic fluctuations, suggesting that alpha-curcumene maintained a well-defined binding pose throughout the simulation. Dihedral PCA (Figure 7D) indicated that the torsional degrees of freedom of the ligand remained confined to energetically favorable conformations, reflecting restricted but stable dynamics during the trajectory.

Further structural descriptors (Figure 7E) supported the stability of the complex. The rGyr remained steady (3.2–3.6 Å), indicating compactness of the protein structure. MolSA and SASA values showed no significant deviation, confirming the absence of unfolding or abnormal solvent exposure during the simulation. The stable SASA further validated sustained hydrophobic interactions between alpha-curcumene and the CYP2E1 binding pocket. The MD results suggest that alpha-curcumene forms a stable and energetically favorable complex with CYP2E1. The observed structural stability, consistent RMSD patterns, and minimal fluctuations highlight its potential as a bioactive compound capable of modulating CYP2E1 activity.

3.3. Protein–ligand interaction analysis

The interaction dynamics of alpha-curcumene within the active site of CYP2E1 were evaluated throughout the 100 ns MD simulation. The two-dimensional interaction diagram (Figure 8A) highlighted the dominant binding residues, including hydrophobic contacts with PHE46, LEU217, and LEU228, as well as a key π–π stacking interaction with TRP214, which persisted for approximately 35% of the simulation time. Interaction fraction analysis (Figure 8B) confirmed the recurrent involvement of residues PHE46, TRP214, and LEU217, indicating their essential role in stabilizing the ligand within the catalytic pocket. The protein–ligand contact timeline (Figure 8C) further revealed continuous hydrophobic interactions with multiple residues, most notably PHE46, TRP214, and LEU217, consistent with the stable RMSD and RMSF profiles observed in the MD trajectory. These findings suggest that the stability of the alpha-curcumene–CYP2E1 complex is largely governed by persistent hydrophobic and aromatic stacking interactions, which anchor the ligand in the active site and contribute to its favorable binding energetics.

3.4. FEL and PCA

To further explore the conformational dynamics of the alpha-curcumene–CYP2E1 complex, PCA and FEL mapping was performed. The 2D FEL plot (Figure 9A) revealed multiple low-energy basins, represented by blue regions, indicating the presence of stable conformational states sampled throughout the 100 ns simulation. The 3D FEL projection (Figure 9B) confirmed the rugged but energetically favorable landscape, with the majority of the conformations clustered around shallow energy minima, suggesting that the protein–ligand complex adopted stable conformations without undergoing large-scale structural transitions.

The 3D PCA projection (Figure 9C) illustrated the distribution of conformations along the first three principal components, with dense clustering reflecting limited global flexibility and stable motion patterns across the simulation trajectory. Probability density function (PDF) analysis (Figure 9D) further confirmed that PC1 and PC2 were normally distributed around central values, indicating restricted fluctuations and consistent sampling of low-energy states. PCA and FEL analyses confirmed that the alpha-curcumene–CYP2E1 complex remained dynamically stable and confined to energetically favorable conformational states throughout the simulation, consistent with RMSD and interaction profile results.

3.5. MM/GBSA binding free energy

The MM/GBSA analysis of the alpha-curcumene–CYP2E1 (3T3Z) complex yielded a mean ΔG_bind of −75.31 ± 3.1, indicating a strongly favorable binding (Figure 10). Decomposition of the energetic terms shows that van der Waals interactions (ΔG_bind_VdW = −50.09 ± 2.1) and lipophilic contributions (−29.75 ± 2.9) are the dominant stabilizing factors, consistent with the hydrophobic/π-stacking contacts observed with PHE46, TRP214, LEU217, and LEU228. Electrostatic/Coulombic interactions (−20.25 ± 2.0) provide additional stabilization, whereas

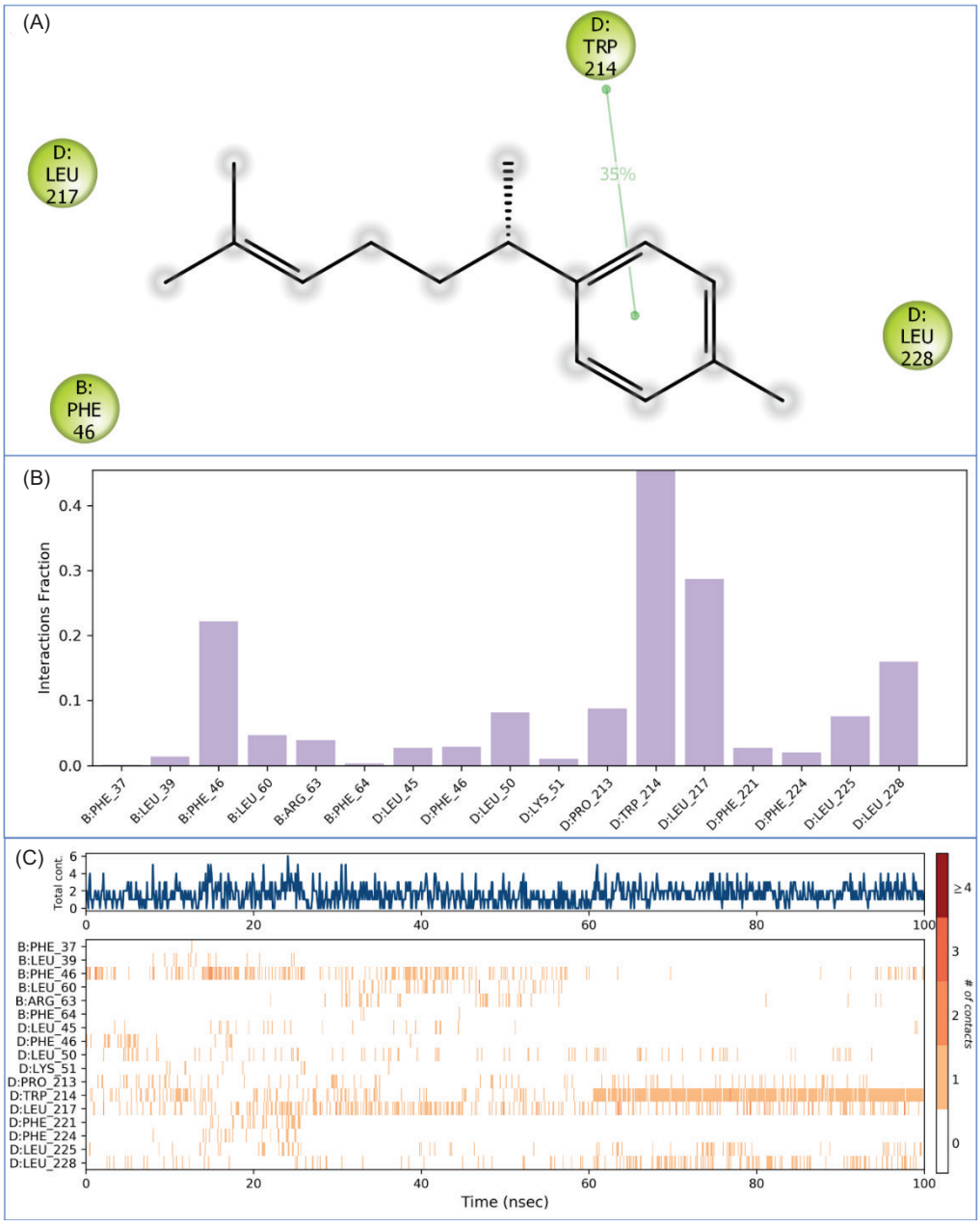

Figure 8. Ligand interaction profile during MD. (A) Major residues interacting with the ligand. (B) Interaction frequency over 100 ns. (C) Time evolution and stability of ligand–residue contacts.

hydrogen-bonding contributions are modest (−2.03 ± 0.99), aligning with a binding mode primarily governed by aromatic and aliphatic packing rather than directional H-bonding. The covalent/bonded term (−4.89 ± 0.8) is small and favorable, suggesting minimal strain upon complex formation.

4. DISCUSSION

The present study investigated the therapeutic potential of phytoconstituents from *Satureja hortensis* L. against urethane-induced mutagenesis, employing a multilayered computational strategy that integrated drug-likeness screening, ADMET profiling, molecular docking, MD simulations, and binding free energy calculations. In the phytochemical context, compositional analyses of *Satureja species* consistently report a terpene-rich essential oil fraction, often including sesquiterpenes such as alpha-curcumene, zingiberene, and related hydrocarbons. These compositional data corroborate the biological plausibility of our candidate selection and indicate that alpha-curcumene is a realistic and abundant constituent to test experimentally for CYP2E1-modulating

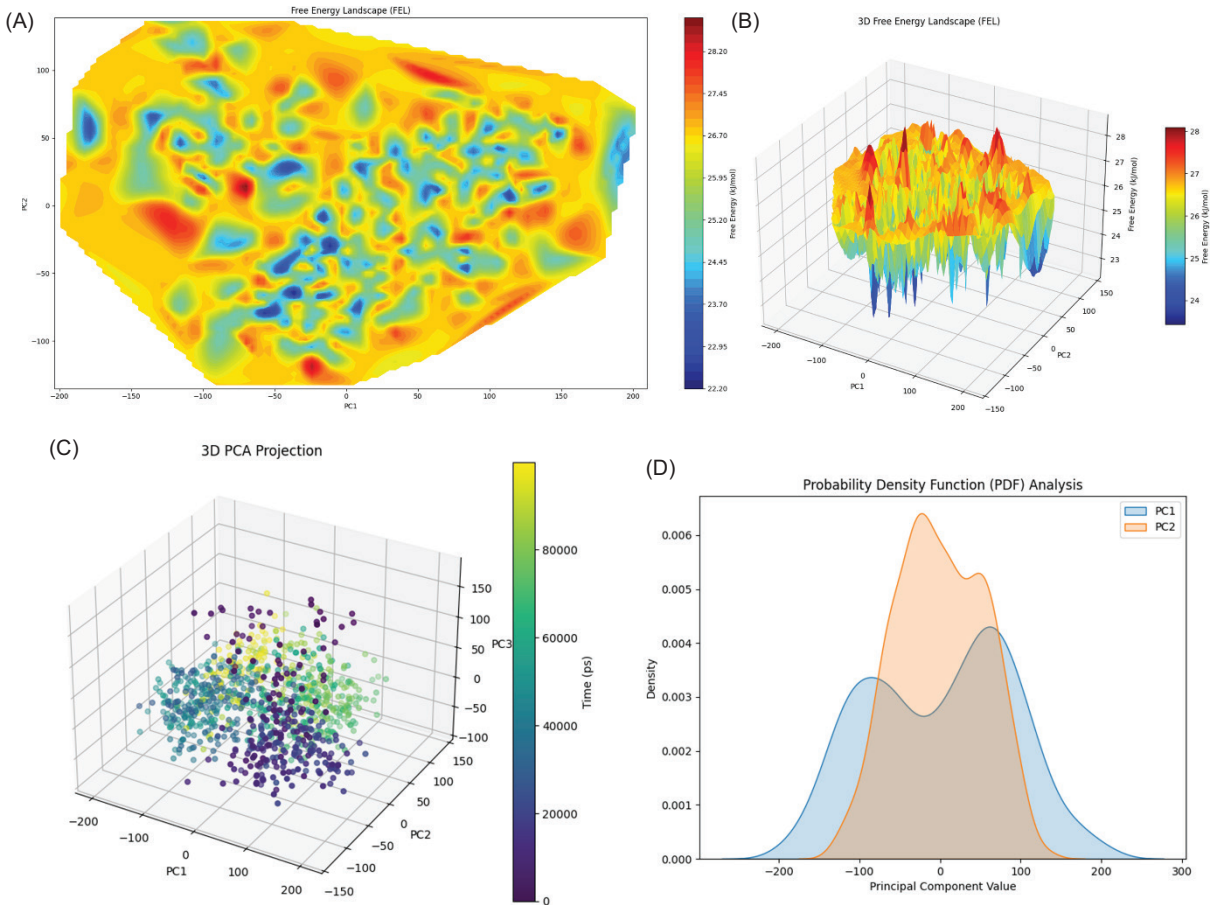

Figure 9. PCA-based free energy and motion analysis of the MD trajectory. (A) 2D free energy landscape (FEL) distribution. (B) 3D FEL showing energy minima and conformational states. (C) 3D PCA projection illustrating conformational clustering over time. (D) Probability density (PDF) plots of PC1 and PC2 showing dominant motions.

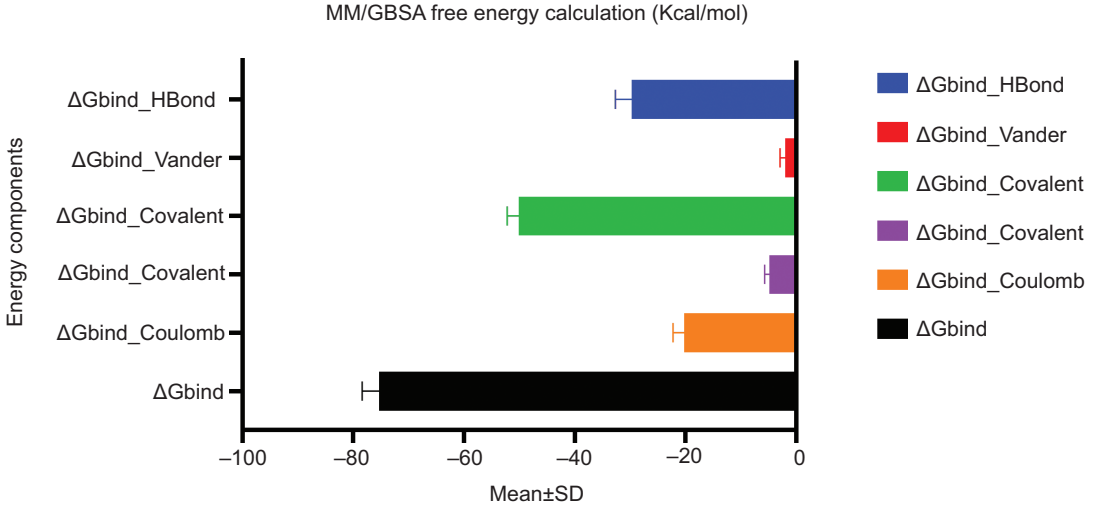

Figure 10. MM/GBSA energy components showing strong overall ligand–protein binding affinity.

and chemopreventive activity (Elmdoustazar et al., 2025; Shariatzadeh et al., 2025) Phytochemical filtering using drug-likeness and ADMET parameters revealed that most terpenoids of *S. hortensis* satisfied Lipinski's rule of five and were free from PAINS structural alerts, suggesting promising drug-like behavior. The predicted high intestinal absorption, favorable blood–brain barrier permeability of certain compounds, and minimal toxicity alerts further underscored their pharmacological relevance.

Among the screened candidates, alpha-curcumene demonstrated superior binding affinity toward CYP2E1 (3T3Z) compared with other phytoconstituents such as bicyclogermacrene, humulene, and beta-caryophyllene. Molecular docking revealed stable hydrophobic and π–π stacking interactions with key residues (PHE46, TRP214, LEU217, and LEU228), consistent with the hydrophobic nature of the enzyme's active site. This preferential binding orientation likely accounts for the higher docking score observed for alpha-curcumene. MD simulation provided further insight into the stability of the alpha-curcumene–CYP2E1 complex. Furthermore, MD simulation parameters provide quantitative insight into the stability and functional relevance of *Satureja hortensis* L. phytoconstituent-target complexes associated with urethane-induced mutagenesis. RMSD confirms conformational stability of bound systems, while RMSF identifies flexible residues influencing active-site accessibility. The rGyr reflects global protein compactness upon ligand binding, and SASA reveals changes in surface exposure affecting ligand retention (De Vivo et al., 2016). Persistent hydrogen bonding and favorable MM/GBSA binding free energies collectively correlate dynamic stability with predicted antimutagenic potential. PCA and FEL mapping further revealed that the alpha-curcumene–CYP2E1 complex sampled multiple low-energy basins while remaining confined to stable conformational states, indicative of robust binding stability.

Our in-silico results showed strong hydrophobic anchoring of alpha-curcumene in the CYP2E1 active site, sustained interaction occupancy with residues such as PHE46 and TRP214, and a favorable MM/GBSA ΔG_bind dominated by van der Waals and lipophilic terms, which are consistent with the literature reporting that terpenoid scaffolds frequently interact with cytochrome P450 enzymes through dispersion-driven hydrophobic and aromatic contacts. Reviews and experimental studies showed that terpenoids and related natural products commonly bind to and inhibit CYP isoforms, often via nonpolar packing rather than extensive hydrogen bonding, which can lead to inhibition or altered metabolic activity (Kamran et al., 2022; Li et al., 2024).

The functional relevance of targeting CYP2E1 for chemoprevention is well established. CYP2E1 has been identified as a principal enzyme responsible for the oxidative metabolism of urethane and other small carcinogens, and CYP2E1 activity is linked to bioactivation pathways that produce reactive metabolites and oxidative stress contributing to mutagenesis (Garciá-Suástegui et al., 2017). Thus, inhibitors of CYP2E1 can attenuate urethane biotransformation and its genotoxic consequences, a mechanism proposed and experimentally supported in prior investigations (Sozio et al., 2021). Our observation that alpha-curcumene adopts a stable binding pose in the CYP2E1 pocket (Figure 11), therefore, aligns mechanistically with the hypothesis that phytochemical inhibition of CYP2E1 can reduce urethane-induced DNA damage (Hoffler et al., 2005).

Various structurally distinct natural products (curcuminoids and other polyphenols) have shown CYP modulation and hepatoprotective effects in in vitro and in vivo

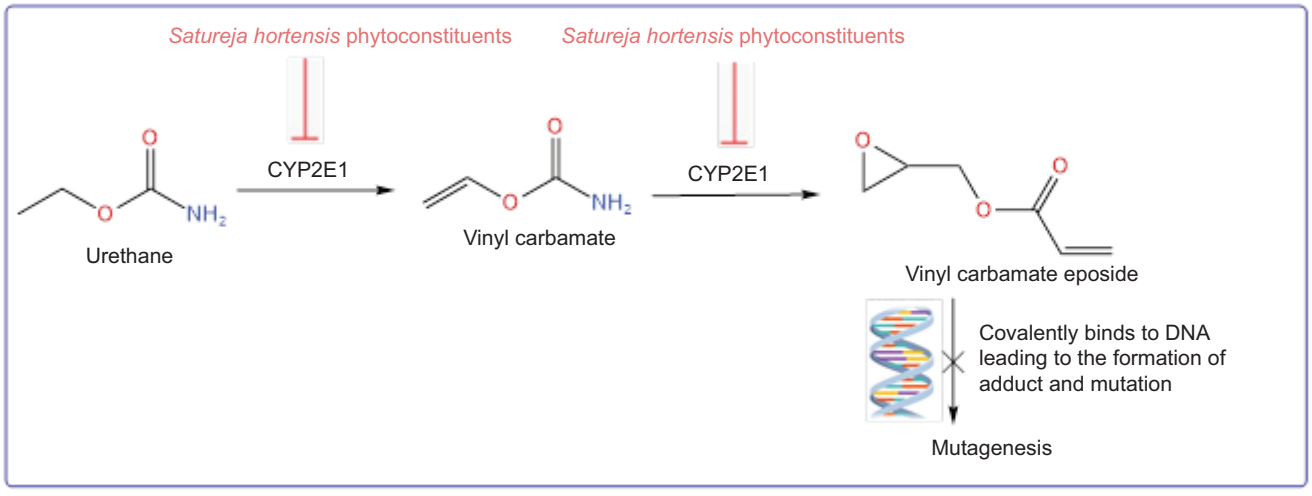

Figure 11. Mechanism of action of phytoconstituents to prevent urethane-induced mutagenesis.

models (Farzaei et al., 2018). Curcuminoids, for example, have repeatedly been reported to interact with and inhibit several CYP isoforms (including modulation of CYP2E1 in some experimental systems), producing protective outcomes against xenobiotic-induced oxidative injury (Castaño et al., 2019). These empirical findings support our computational inference that natural products with hydrophobic/aromatic character can exert notable effects on CYP2E1 function and consequent toxicant metabolism; alpha-curcumene's strong van der Waals and lipophilic binding signature mirrors those mechanisms.

5. LIMITATION OF THE STUDY

While our data position alpha-curcumene as a promising lead with favorable ADMET predictions and robust dynamic stability, the literature emphasizes that in vitro enzyme assays, hepatocellular models, and in vivo mutagenesis studies are required to confirm inhibition of CYP2E1-mediated urethane activation and assess potential off-target effects or drug–herb interactions (Cho and Yoon, 2015; Naeem et al., 2022).

6. CONCLUSION

This study highlights the pharmacological potential of *Satureja hortensis* L. phytoconstituents, with alpha-curcumene emerging as the most potent CYP2E1 inhibitor. The compound displayed drug-like properties, favorable ADMET characteristics, strong docking interactions, and exceptional dynamic stability confirmed by MD and MM/GBSA analyses. These results suggest that alpha-curcumene could mitigate urethane-induced mutagenesis via CYP2E1 inhibition. Future experimental investigations are essential to validate these computational predictions and advance alpha-curcumene as a candidate for chemopreventive strategies.

MANDATORY DISCLOSURE ON USE OF ARTIFICIAL INTELLIGENCE

XXX

AUTHOR CONTRIBUTIONS

Vindya NS formulated the research concept and design, collection and/or assembly of data, data analysis and interpretation, and writing of the article; Syed Sagheer Ahmed was involved with the research concept and design, and the final approval of the article; Bharathi DR was responsible for data analysis and interpretation, and critical revision of the article.

ACKNOWLEDGEMENT

XXX

CONFLICTS OF INTEREST

The authors declare no conflicts of interests.

DATA AVAILABILITY

Data will be made available on request.

FUNDING

Not available.

ETHICAL APPROVAL

Not applicable.

ORCID

Vindya NS	0000-0001-6552-7522
Syed Sagheer Ahmed	0000-0001-9817-9747
Bharathi DR	0000-0002-8153-2839

REFERENCES

Baell, J.B., & Nissink, J.W.M. 2018. Seven year itch: Pan-assay interference compounds (PAINS) in 2017—Utility and limitations, ACS Chemical Biolog., 13(1), 36–44. https://doi.org/10.1021/acschembio.7b00903.

C, P. et al. 2025 Repurposing terfenadine and domperidone for inhibition of apoptotic gene association in colorectal cancer: A system pharmacology approach integrated with molecular docking, MD simulations, and post-MD simulation analysis. Bioinformatics and Biology Insights. 19(July), 1–21. https://doi.org/10.1177/11779322251365019.

Castaño, P.R., Parween, S., & Pandey, A.V. 2019. Bioactivity of curcumin on the cytochrome P450 enzymes of the steroidogenic pathway. International Journal of Molecular Sciences. 20(18), 1–21. https://doi.org/10.3390/ijms20184606.

Chambre, D.R. et al. 2020. Chemical composition, antioxidant capacity, and thermal behavior of Satureja hortensis essential oil. Scientific Reports. 10(1), 1–12. https://doi.org/10.1038/s41598-020-78263-9.

Cho, H.J., & Yoon, I. S. 2015. Pharmacokinetic interactions of herbs with cytochrome p450 and p-glycoprotein. Evidence-based Complementary and Alternative Medicine. 2015, 1–10. https://doi.org/10.1155/2015/736431.

DeVore, N.M. et al. 2012. Structural comparison of cytochromes P450 2A6, 2A13, and 2E1 with pilocarpine. FEBS Journal. 279(9), 1621–1631. https://doi.org/10.1111/j.1742-4658.2011.08412.x.

Elmdoustazar, P. et al. 2025. Phytochemical traits and biological activity of Satureja hortensis and Satureja macrantha as culinary spices using GC–MS/MS and LC–MS/MS Techniques. Food Science and Nutrition. 13(8), 1–22. https://doi.org/10.1002/fsn3.70733.

Farzaei, M.H. et al. 2018. Curcumin in liver diseases: A systematic review of the cellular mechanisms of oxidative stress and clinical perspective. Nutrients. 10(7), 1–28. https://doi.org/10.3390/nu10070855.

Fierascu, I. et al. 2018. Phytochemical profile and biological activities of Satureja hortensis l.: A review of the last decade. Molecules 23(10), 1–19. https://doi.org/10.3390/molecules23102458.

Garciá-Suástegui, W.A. et al. 2017. The Role of CYP2E1 in the drug metabolism or bioactivation in the brain. Oxidative Medicine and Cellular Longevity. 2017, 1–14. https://doi.org/10.1155/2017/4680732.

Gote, S. et al. 2025. In silico investigation of coumarin-based compounds targeting Keap1-Nrf2 pathway involved in the development of Alzheimer's disease. Letters in Drug Design & Discovery. 22(46), 69241–69274. https://doi.org/10.2174/0115701808338518241224060020.

Guengerich, F.P. 2020. Cytochrome P450 2E1 and its roles in disease. Chemico-Biological Interactions. 322, 109056. https://doi.org/10.1016/j.cbi.2020.109056.

Hoffler, U. et al. 2005. Inhibition of urethane-induced genotoxicity and cell proliferation in CYP2E1-null mice. Mutation Research—Fundamental and Molecular Mechanisms of Mutagenesis, 572(1–2), pp. 58–72. https://doi.org/10.1016/j.mrfmmm.2004.12.005.

Iacopetta, D. et al. 2023. Impact of cytochrome P450 enzymes on the phase I metabolism of drugs. Applied Sciences. 13(10), 1–21. https://doi.org/10.3390/app13106045.

Ivanović, V. et al. 2020. Lipinski's rule of five, famous extensions and famous exceptions. Popular Scientific Article. 3(1), 171–177.

Joshi, K.R. et al. 2025. Validation of antidiabetic potential of Pterocarpus marsupium: An in silico approach. Journal of Chemistry. Edited by S. Basu Roy, 2025(1), pp. 1–18. https://doi.org/10.1155/joch/3829977.

Kamaria, P. et al. 2025. Evaluation of Quercus infectoria phytoconstituents against oral cancer: Network pharmacology, docking simulation, and in vitro cytotoxicity assay. Food Science and Nutrition. 13(9), 1–23. https://doi.org/10.1002/fsn3.70857.

Kamran, S. et al. 2022. Therapeutic potential of certain terpenoids as anticancer agents: A scoping review. Cancers. 14(5), 1–46. https://doi.org/10.3390/cancers14051100.

Kiran, S. et al. 2025. Integrated computational approach revealed the potential inhibitory effect of xanthone derivatives against Marburg virus nucleocapsid. VirusDisease. 3(August), 415–427. https://doi.org/10.1007/s13337-025-00933-x.

Kumar, R. et al. 2025. Molecular docking , drug—likeness properties, and toxicity prediction of alkaloidal phytoconstituents of piper longum against monoamine oxidase enzymeA as an antidepressive agent. Discover Chemistry. 2(23), 1–18. doi: https://doi.org/10.1007/s44371-025-00188-x.

Kumburovic, I. et al. 2020. Antioxidant effects of satureja hortensis L. attenuate the anxiogenic effect of cisplatin in rats. Oxidative Medicine and Cellular Longevity. 2019, 1–15. https://doi.org/10.1155/2019/8307196.

Li, D. et al. 2024. Triterpenoids from Ganoderma lucidum inhibit cytochrome P450 enzymes interfering with the metabolic process of specific clinical drugs. Frontiers in Pharmacology. 15, 1–15. https://doi.org/10.3389/fphar.2024.1485209.

Naeem, A. et al. 2022. Natural products as anticancer agents: Current status and future perspectives. Molecules. https://doi.org/10.3390/molecules27238367.

Oliveira, V.C. et al. 2020. Betulinic acid modulates urethane-induced genotoxicity and mutagenicity in mice and Drosophila melanogaster. Food and Chemical Toxicology. 138(December 2019), 111228. https://doi.org/10.1016/j.fct.2020.111228.

Pandey, B. et al. 2024. LC-MS profiling and cytotoxic activity of Angiopteris helferiana against HepG2 cell line: Molecular insight to investigate anticancer agent. PLoS ONE. 19(12), 1–24. https://doi.org/10.1371/journal.pone.0309797.

Pant, L. et al. 2024. In Silico and in vitro studies of antibacterial activity of cow urine distillate (CUD). Evidence-based Complementary and Alternative Medicine. 2024(1), 1–10. https://doi.org/10.1155/2024/1904763.

Park, S.R. et al. 2009. Exposure to ethyl carbamate in alcohol-drinking and nondrinking adults and its reduction by simple charcoal filtration. Food Control. 20(10), 946–952. https://doi.org/10.1016/j.foodcont.2009.02.006.

Prasad, S. et al. 2025. Molecular docking and pharmacokinetic evaluations of curcuminbased scaffolds as MDM2p53 inhibitors', *Discover Chemistry*, 2(53), 1–18. https://doi.org/10.1007/s44371-025-00128-9.

Reed, L., Arlt, V.M., & Phillips, D.H. 2018. The role of cytochrome P450 enzymes in carcinogen activation and detoxication: An in vivo-in vitro paradox. Carcinogenesis 39(7), 851–859. https://doi.org/10.1093/carcin/bgy058.

Saritha, K., Alivelu, M., & Mohammad, M. 2024. Drug-likeness analysis, in silico ADMET profiling of compounds in Kedrostis foetidissima (Jacq.) Cogn, and antibacterial activity of the plant extract. In Silico Pharmacology. 12(2), 1–11. https://doi.org/10.1007/s40203-024-00240-1.

Schlatter, J., & Lutz, W.K. 1990. The carcinogenic potential of ethyl carbamate (urethane): Risk assessment at human dietary exposure levels. Food and Chemical Toxicology. 28(3), 205–211. https://doi.org/10.1016/0278-6915(90)90008-B.

Shariatzadeh, S., Talebi, S.M., & Ghorbanpour, M. 2025. Variability in seed essential oil composition of the cultivated Satureja hortensis L. (Lamiaceae) populations in Iran. BMC Plant Biology. 25(1), 1–13. https://doi.org/10.1186/s12870-025-07136-y.

Sozio, F. et al. 2021. *Urethane-induced lung carcinogenesis*. 1st edn, *Methods in Cell Biology*. 1st edn. Elsevier Inc. https://doi.org/10.1016/bs.mcb.2020.09.005.

Thapa, S. et al. 2023. In-silico investigation and drug likeliness studies of benzimidazole congeners: The new face of innovation. Informatics in Medicine Unlocked. 38(January), 101213. https://doi.org/10.1016/j.imu.2023.101213.

Thapa, S. et al. 2024. Synthesis, molecular docking, molecular dynamic simulation studies, and antitubercular activity

evaluation of substituted benzimidazole derivatives. Advances in Pharmacological and Pharmaceutical Sciences. 2024, 1–25. https://doi.org/10.1155/2024/9986613.

Thapa, S., Nargund, S.L., & Biradar, M.S. 2023. Molecular design and in-silico analysis of trisubstituted benzimidazole derivatives as Ftsz inhibitor. Journal of Chemistry. Edited by F. Polticelli, 2023(7), 1–9. https://doi.org/10.1155/2023/9307613.

Trott, O., & Olson, A.J. 2009. AutoDock Vina: Improving the speed and accuracy of docking with a new scoring function, efficient optimization, and multithreading. Journal of Computational Chemistry. 31(2), 455–461. https://doi.org/10.1002/jcc.21334.

Vivek-Ananth, R.P. et al. 2023. IMPPAT 2.0: An enhanced and expanded phytochemical atlas of Indian medicinal plants. ACS Omega. 8(9), 8827–8845. https://doi.org/10.1021/acsomega.3c00156.

De Vivo, M. et al. 2016. Role of molecular Dynamics and Related Methods in Drug Discovery', *Journal of Medicinal Chemistry*, 59(9), 4035–4061. https://doi.org/10.1021/acs.jmedchem.5b01684.

Vladić, J. et al. 2020. Evaluation of anticancer activity of Satureja Montana supercritical and spray-dried extracts on Ehrlich's ascites carcinoma bearing mice. Plants. 9(11), 1–14. https://doi.org/10.3390/plants9111532.

Xiong, G. et al. 2021. ADMETlab 2.0: An integrated online platform for accurate and comprehensive predictions of ADMET properties. Nucleic Acids Research. 49(W1), W5–W14. https://doi.org/10.1093/nar/gkab255.

Zuckerman, A.J. 1995. IARC monographs on the evaluation of carcinogenic risks to humans. Journal of Clinical Pathology. 48(7), 691–691. https://doi.org/10.1136/jcp.48.7.691-a.

SUPPLEMENTARY FILE

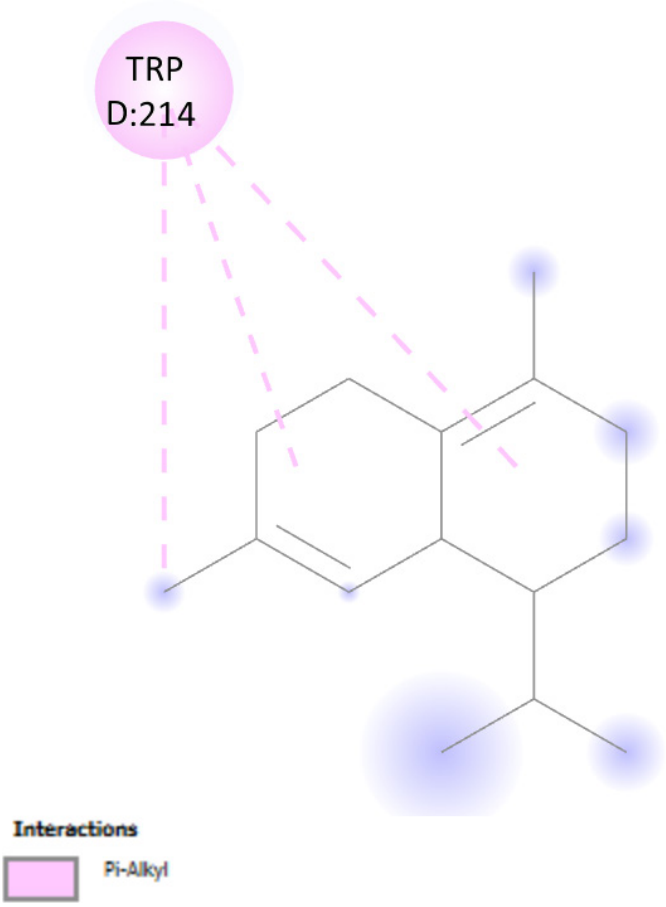

Figure 1S. 2D molecular interaction of (+)-delta-cadinene against human cytochrome P450 2E1 in complex with pilocarpine (3T3Z).

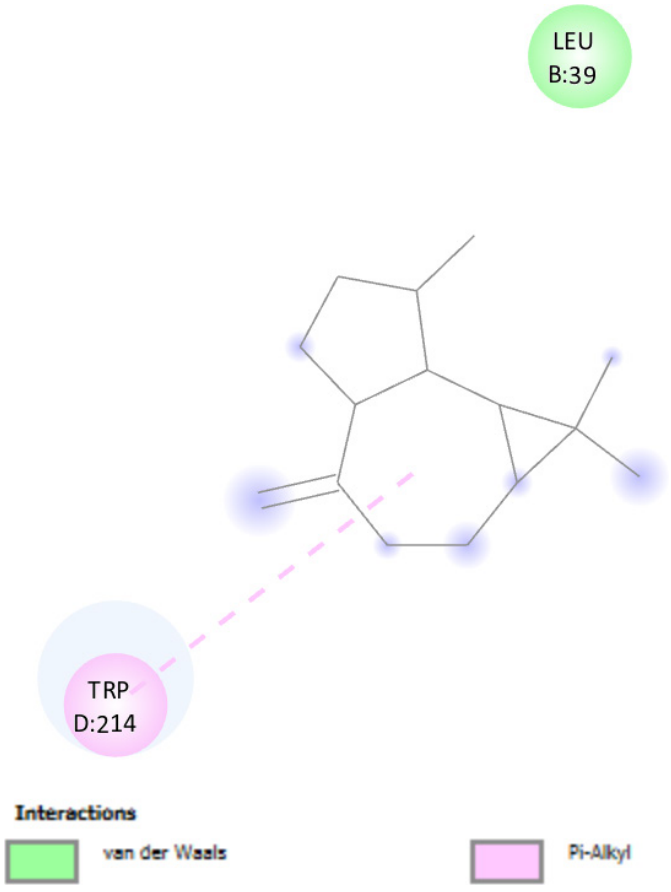

Figure 2S. 2D molecular interaction of allo-aromadendrene against human cytochrome P450 2E1 in complex with pilocarpine (3T3Z).

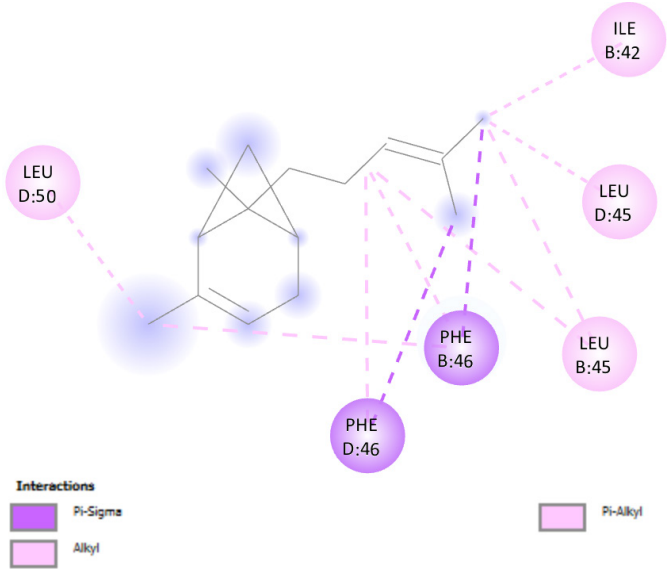

Figure 3S. 2D molecular interaction of alpha-bergamotene against human cytochrome P450 2E1 in complex with pilocarpine (3T3Z).

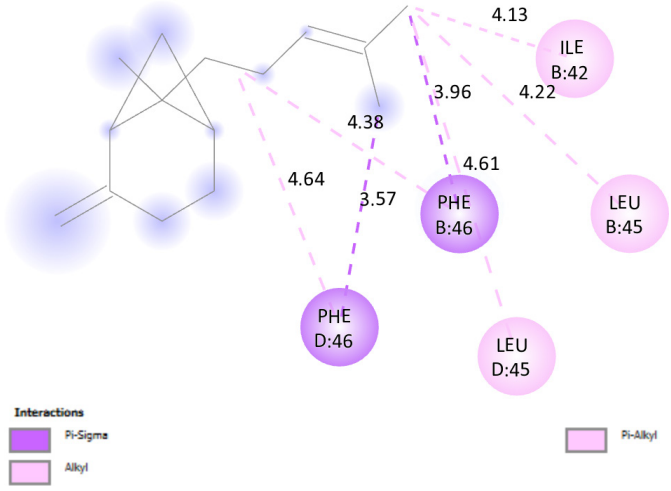

Figure 4S. 2D molecular interaction of bergamotene against human cytochrome P450 2E1 in complex with pilocarpine (3T3Z).

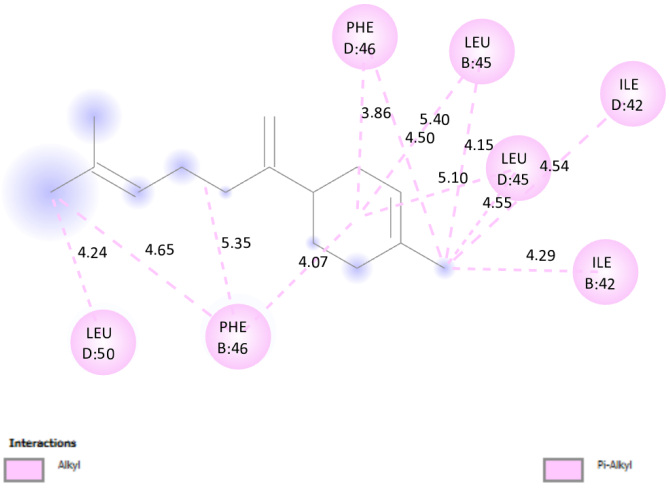

Figure 5S. 2D molecular interaction of beta-bisabolene against human cytochrome P450 2E1 in complex with pilocarpine (3T3Z).

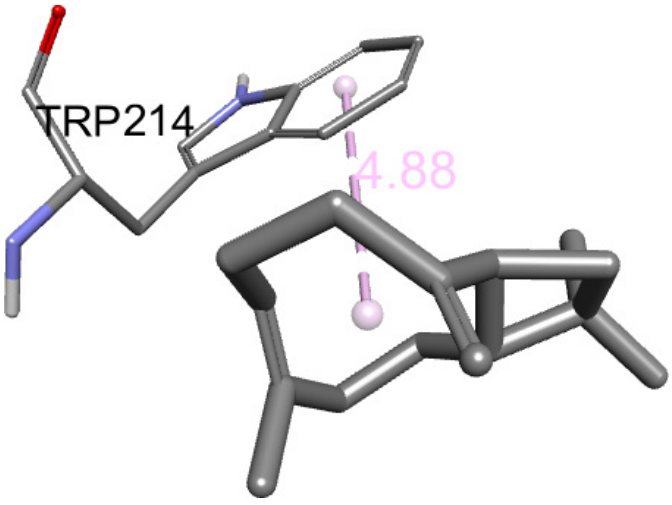

Figure 6S. 3D molecular interaction of beta-caryophyllene against human cytochrome P450 2E1 in complex with pilocarpine (3T3Z).

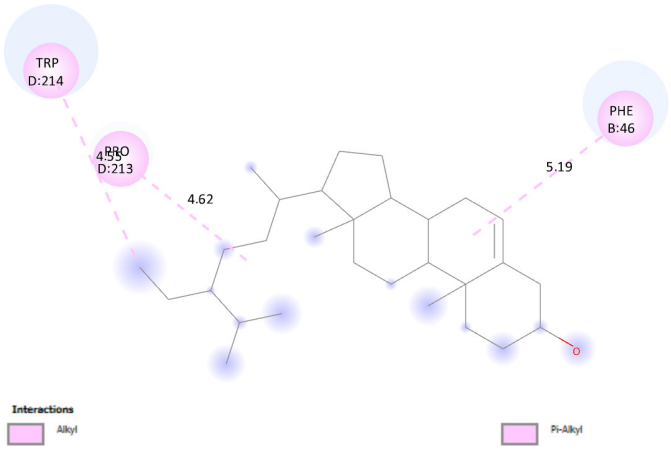

Figure 7S. 2D molecular interaction of beta-sitosterol against human cytochrome P450 2E1 in complex with pilocarpine (3T3Z).

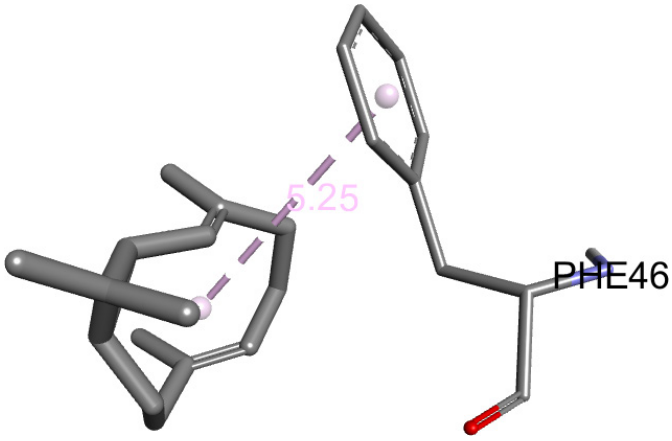

Figure 8S. 3D molecular interaction of bicyclogermacrene against human cytochrome P450 2E1 in complex with pilocarpine (3T3Z).

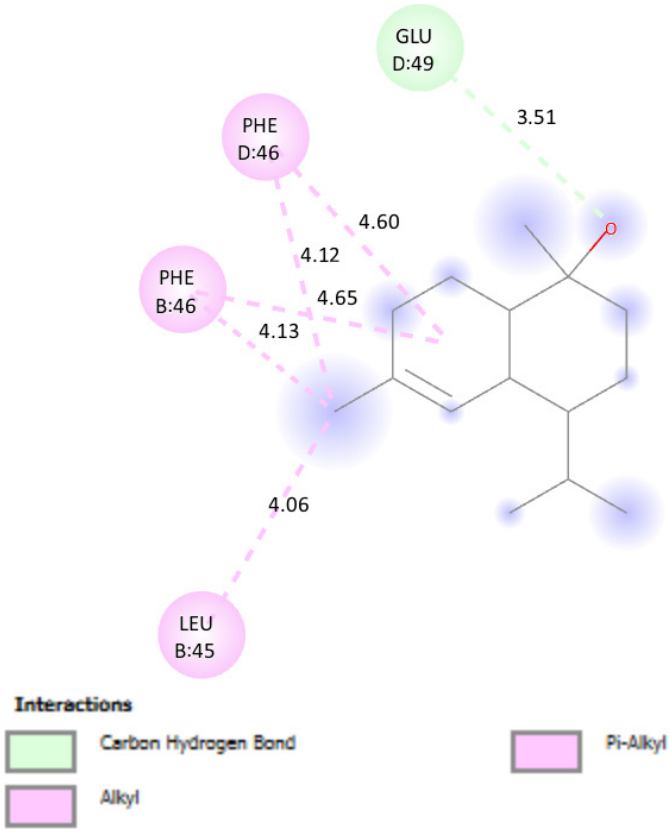

Figure 9S. 2D molecular interaction of cedrelanol against human cytochrome P450 2E1 in complex with pilocarpine (3T3Z).

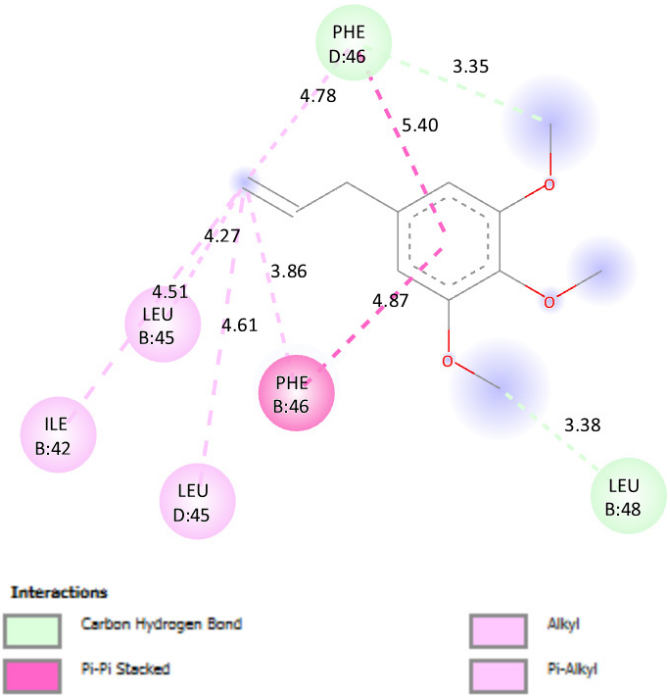

Figure 10S. 2D molecular interaction of elemicin against human cytochrome P450 2E1 in complex with pilocarpine (3T3Z).

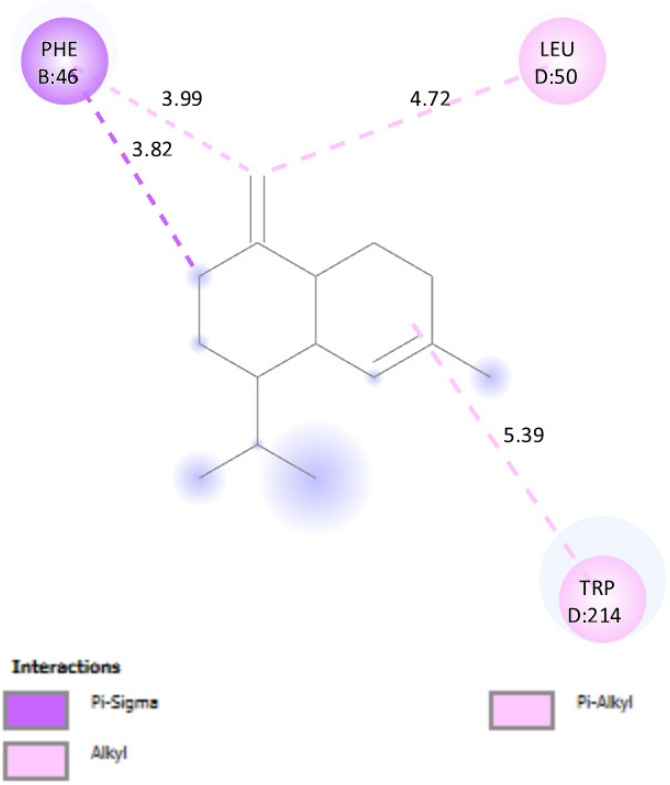

Figure 11S. 2D molecular interaction of gamma-muurolene against human cytochrome P450 2E1 in complex with pilocarpine (3T3Z).

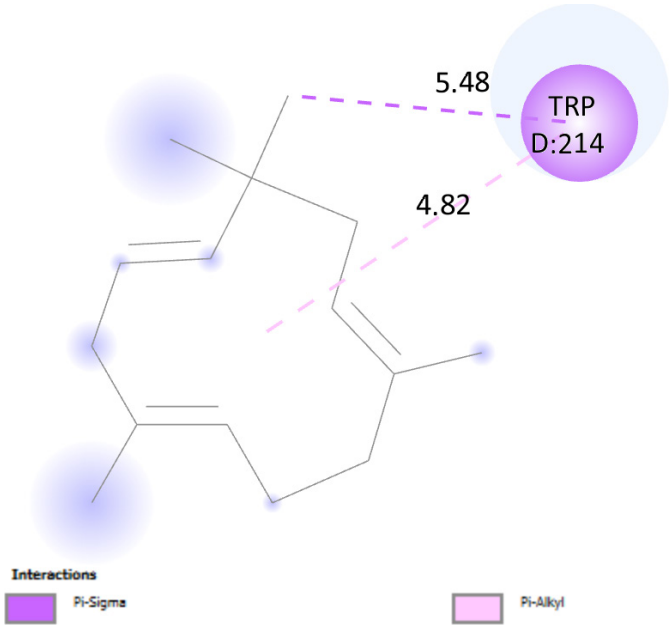

Figure 12S. 2D molecular interaction of humulene against human cytochrome P450 2E1 in complex with pilocarpine (3T3Z).

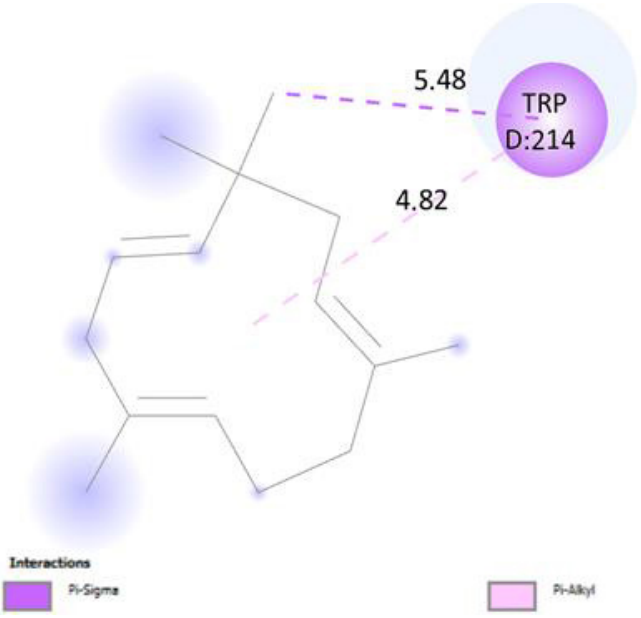

Figure 13S. 2D molecular interaction of humulene epoxyde against human cytochrome P450 2E1 in complex with pilocarpine (3T3Z).

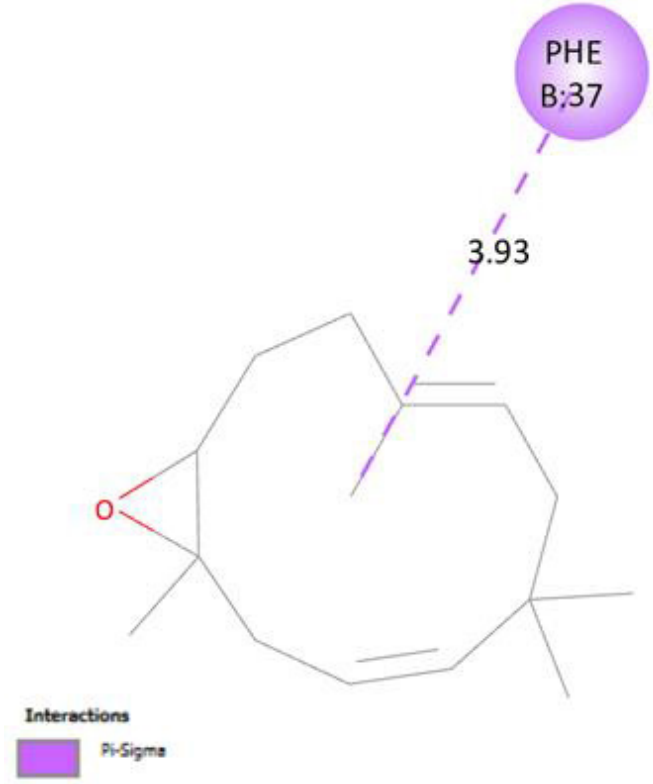

Figure 14S. 2D molecular interaction of nerolidol against human cytochrome P450 2E1 in complex with pilocarpine (3T3Z).

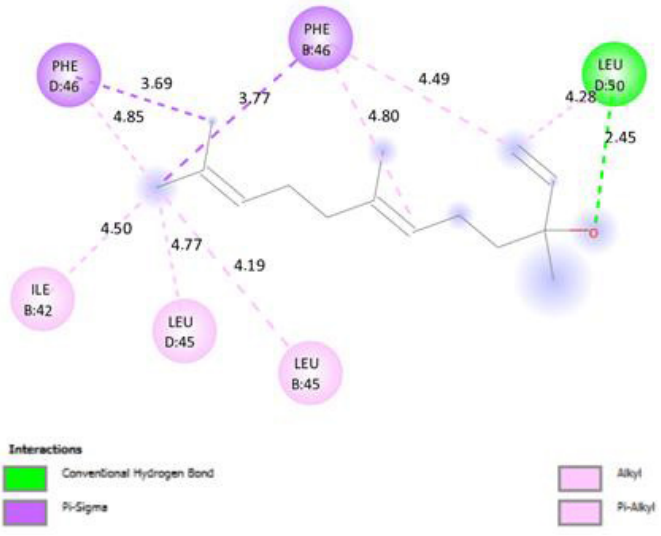

Figure 15S. 2D molecular interaction of viridiflorene against human cytochrome P450 2E1 in complex with pilocarpine (3T3Z).

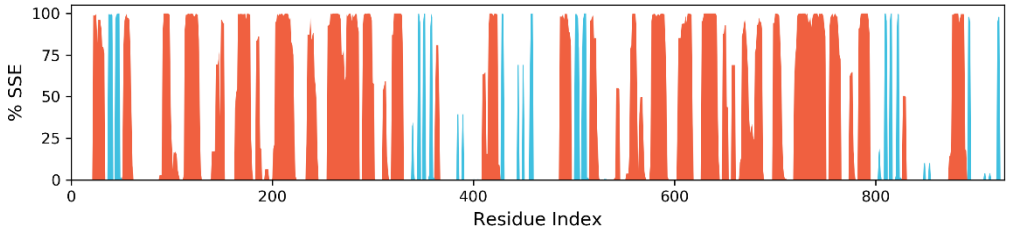

Figure 16S. SEE histogram of protein human cytochrome P450 2E1 in complex with pilocarpine (3T3Z) during 100 ns MD simulation.

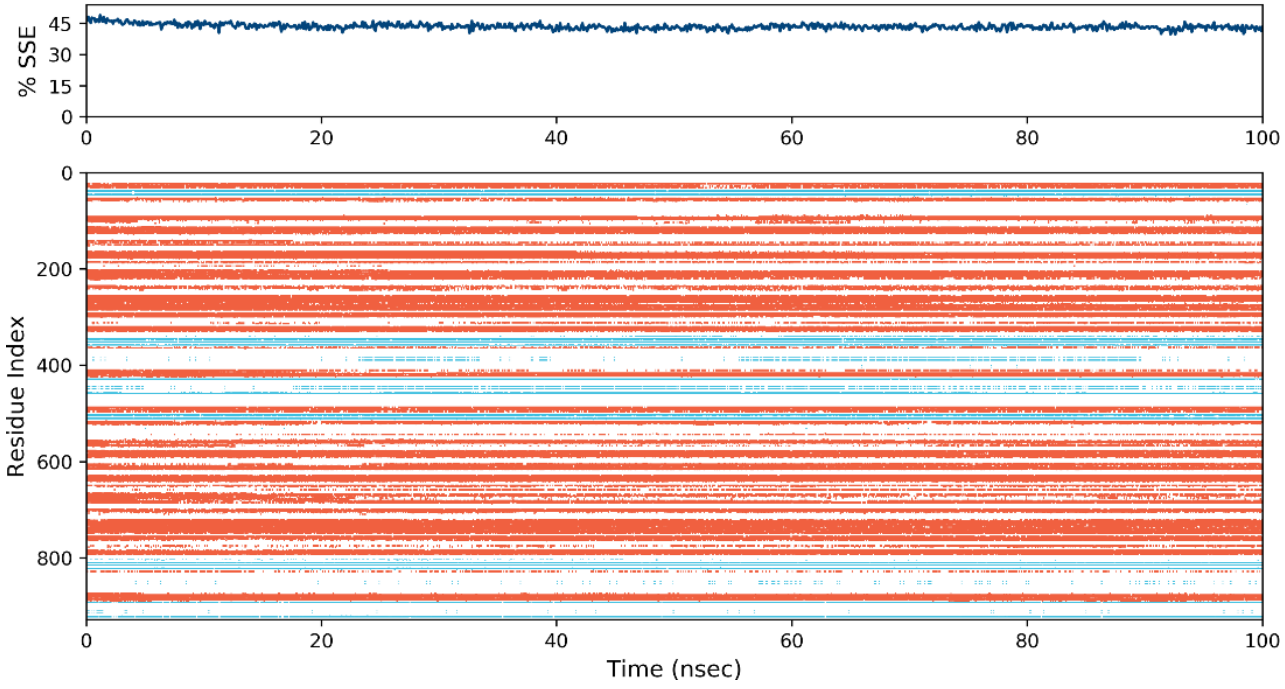

Figure 17S. SEE timeline of protein human cytochrome P450 2E1 in complex with pilocarpine (3T3Z) during 100 ns MD simulation.